SCIENCE CHINA Materials ARTICLES

mater.scichina.com link.springer.com https://doi.org/10.1007/s40843-025-3599-5

SPECIAL ISSUE: 2026 Emerging Investigator Issue

Tellurium vacancy-rich Bi_2Te_3 as a high-performance cathode material for aqueous zinc ion storage

Zhoujie Tang[1], Wenshu Chen[1*], Zhilong Deng[1], Ziyue Zhu[1], Haoyuan Meng[1], Na Ju[1], Fei Ye[2], Yongping Du[3], Yuping Wu[4,5] and Linfeng Hu[1,5*]

ABSTRACT Layered transition metal tellurides (TMT) show potential for development into high-performance cathode materials for aqueous zinc ion batteries, yet their holistic performance metrics (e.g., specific capacity, rate capability, stability) remain substantially distant from practical utilization. Herein, we employed a straightforward and efficient $NaBH_4$-assisted chemical etching method to generate abundant Te vacancies on the surface of Bi_2Te_3 (termed H-Bi_2Te_3). Our experimental and theoretical investigations reveal that these abundant Te vacancies refine the band structure of H-Bi_2Te_3, enhance its electrical conductivity, and remarkably decrease the diffusion barrier for zinc ions. Moreover, these Te vacancies offer increased storage sites for Zn ions. Consequently, the H-Bi_2Te_3 material showcased superior performance in zinc-ion storage, exhibiting rapid zinc storage kinetics ($D_{Zn^{2+}}$ of 3.98×10^{-11} cm^2 s^{-1}), a noteworthy specific capacity (325 mAh g^{-1} at 0.1 A g^{-1}), impressive rate characteristics (217 mAh g^{-1} at 1 A g^{-1}), and exceptional cyclic stability (retaining a capacity of 70 mAh g^{-1} after 10000 cycles at 1 A g^{-1}). This work not only presents a novel strategy focused on vacancy defect engineering on TMT-based cathode materials in AZIBs, but also opens up possibilities for exploring broader applications of vacancy-rich TMT materials.

Keywords: aqueous zinc ion storage, transition metal tellurides, chemical etching, atomic vacancy, enhanced performance

INTRODUCTION

The evolution of technology has spurred a heightened demand for energy storage solutions. Among these, electrochemical energy storage techniques stand out due to their superior energy density, adaptability, scalability, and multifaceted application domains [1]. Presently, lithium-ion batteries (LIBs) dominate the market as the most established form of electrochemical energy storage. However, concerns related to their safety and environmental impact are driving the pursuit of safer and more sustainable alternatives, particularly for large-scale and high-safety applications like data centers [2]. Aqueous zinc ion batteries (AZIBs) have garnered significant research interest owing to their intrinsic safety, cost-effectiveness, eco-friendliness, and the high energy density of zinc metal (820 mAh g^{-1} and 5854 mAh cm^{-3}) [3,4]. Moreover, they offer straightforward manufacturing processes [5]. Yet, the larger ionic radius and elevated valence state of zinc ions often result in sluggish storage kinetics within cathode materials [6]. This makes the cathode material a pivotal determinant of the overall energy density and rate performance of AZIBs. Consequently, there is an increasing emphasis on developing cathode materials that boast both high specific capacity and rate performance, marking a key area of investigation in AZIB research [7,8].

Over recent years, significant advancements have been made in the development of AZIB cathode materials. These include inorganic manganese and vanadium-based oxides/sulfides [9], metal/covalent organic frameworks [10], polyaniline [11], vanadium phosphate oxide [12], and Prussian blue analogues (PBAs) [13]. Most notably, transition metal chalcogenides such as VSe_2 [14], MoS_2 [15], VS_2 [16], Bi_2S_3 [17] and Bi_2Se_3 [18] have garnered considerable interest due to their unique properties. Their graphite-like layered structures and weak interlayer van der Waals interactions provide a substantial lattice region with rapid electrochemical reaction kinetics. This makes them highly conducive to ion transport and storage, thus making them potential cathode materials for AZIBs. Furthermore, transition metal tellurides (TMTs) often exhibit metallic or semi-metallic properties [19], resulting in significantly superior electrical conductivity compared to other transition metal chalcogenides and oxides. Consequently, they hold great promise as high-performance cathode materials for aqueous zinc ion storage [20,21]. However, the energy storage performance of TMTs in batteries, as reported in the literature, leaves much to be desired [22]. Their specific capacities are notably low, ranging from 165 mAh g^{-1} (at 0.5 A g^{-1}) [23] to 200 mAh g^{-1} (at 0.2 A g^{-1}) [24]. Additionally, both their rate performance and cyclic stability require further enhancement.

To improve the energy storage performance of aqueous zinc-

---

[1] School of Materials Science and Engineering, Southeast University, Nanjing 211189, China
[2] Nanjing Polytechnic Institute, Nanjing 210048, China
[3] MIIT Key Laboratory of Semiconductor Microstructure and Quantum Sensing, Department of Applied Physics, Nanjing University of Science and Technology, Nanjing 210094, China
[4] School of Energy and Environment, Southeast University, Nanjing 211189, China
[5] Z Energy Storage Center, Southeast University, Nanjing 211189, China
[*] Corresponding author (email: 101013800@seu.edu.cn; linfenghu@seu.edu.cn)

ion battery cathode materials, several modification strategies have been proposed. These include doping [25], compounding [26], intercalation [27], and vacancy defect engineering [28]. Notably, the introduction of vacancy defects is a prevalent modification strategy in oxide or chalcogenide cathode materials [29]. Vacancy defects often alter the band structure by introducing impurity bands, ultimately leading to the closure of the band gap [30]. This alteration can enhance its electronic conductivity to a certain degree, thereby improving ion storage kinetics [31]. Furthermore, vacancy defects can serve as ion adsorption sites, thereby enhancing the ion storage specific capacity [32]. The methods for introducing vacancy defects that have been reported include high-temperature calcination [33], irradiation [34], and mechanical ball milling [35]. However, these processes are often complex, and the density of vacancy defects is not easily controllable. Consequently, it is crucial to explore a simple, efficient, and controllable method for creating vacancies.

In this work, we have developed a simple one-step chemical etching method for creating Te vacancy defects in Bi_2Te_3. This approach began with treating Bi_2Te_3 with a $NaBH_4$ solution that led to the chemical etching of surface Te atoms on the layered Bi_2Te_3, subsequently enriching the material with an abundance of Te vacancies (denoted as H-Bi_2Te_3). Our results show that the defective H-Bi_2Te_3 material has superior Zn-ion storage performance compared to pristine (untreated) Bi_2Te_3, demonstrating rapid zinc storage kinetics with a Zn^{2+} diffusion coefficient of approximately 3.98×10^{-11} $cm^2\ s^{-1}$, a high specific capacity of 325 mAh g^{-1} at 0.1 A g^{-1}, robust rate performance maintaining 195 mAh g^{-1} at 2 A g^{-1}, and exceptional cyclic stability with a capacity retention of 70 mAh g^{-1} after 10000 cycles at 2 A g^{-1}. We propose that the increased zinc storage reaction kinetics significantly enhances the material's zinc storage performance. Using a combination of experimental results and theoretical calculations, we have clarified the mechanisms underlying the improved zinc storage reaction kinetics. On one hand, the H-Bi_2Te_3, which has rich Te vacancy defects, exhibits metallicity, while the Bi_2Te_3 without Te vacancies is semiconducting. As a result, the electrical conductivity of the defective H-Bi_2Te_3 improves, promoting the reaction kinetics of Zn-ion storage. Moreover, theoretical calculations indicate that the migration barrier of Zn ions in the defective H-Bi_2Te_3 is significantly reduced, further enhancing the kinetic performance of zinc ion storage. This research provides a straightforward and feasible approach for vacancy defect engineering in transition metal tellurides, offering a practical basis for their use as high-performance cathode materials in AZIBs.

RESULTS AND DISCUSSION

Synthesis and characterizations of defective H-Bi_2Te_3 nanosheets

Fig. 1a schematically shows the synthetic process of the Te vacancy-rich Bi_2Te_3 nanosheet materials. Briefly, we first synthesized Bi_2Te_3 nanosheets via a hydrothermal approach. Then, we employed a $NaBH_4$-assisted chemical etching method to generate abundant Te vacancies on the surface of the prepared Bi_2Te_3 nanosheets, yielding the desired defective Bi_2Te_3 nanosheets (termed H-Bi_2Te_3). The detailed preparation process can be found in the EXPERIMENTAL SECTION.

We first studied the crystal structure of the prepared Bi_2Te_3 (pristine, untreated) and defective H-Bi_2Te_3 (treated). Fig. 1b and Table S1 present the collected and Rietveld-refined X-ray diffraction (XRD) data of pristine Bi_2Te_3 and H-Bi_2Te_3, respectively. The diffraction peaks at 17.48°, 27.74°, 28.84°, 37.92°, and

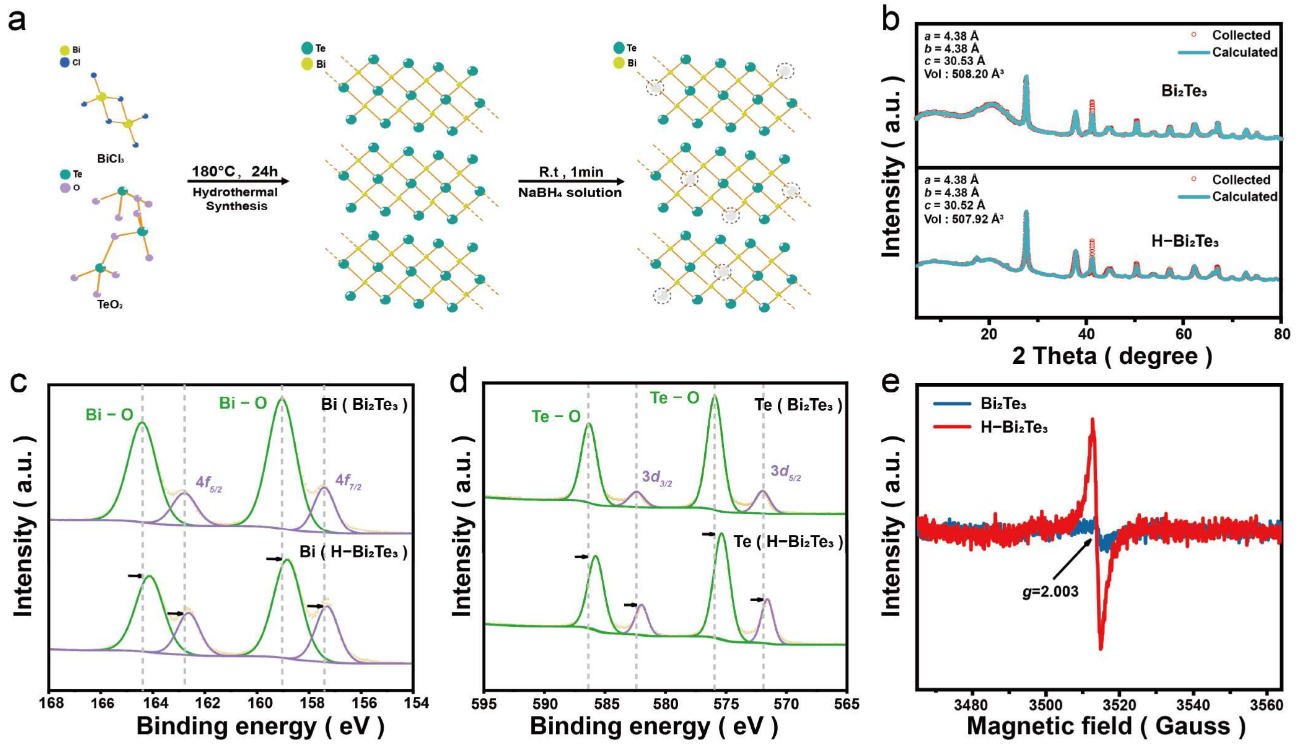

Figure 1 (a) Schematic of the synthetic process of defective H-Bi_2Te_3 nanosheet materials. (b) Rietveld-refined XRD spectra, (c) high-resolution Bi 4f XPS spectra, (d) high-resolution Te 3d XPS spectra, and (e) EPR profiles of the synthesized defective H-Bi_2Te_3 and pristine Bi_2Te_3 materials.

41.30° correspond to the (006), (104), (015), (1010) and (110) crystal planes of the hexagonal phase of Bi_2Te_3 (PDF#82-0358, with lattice constants $a = b = 4.38$ Å, and $c = 30.53$ Å). The XRD and Raman spectra (Fig. S1) indicate that the introduction of vacancies does not alter the crystal structure of Bi_2Te_3. However, we find that the nanosheets treated with $NaBH_4$ exhibit a slight reduction in cell parameters and volume, demonstrating that the Bi–Te bonding strength in the crystal lattice of H-Bi_2Te_3 becomes stronger with the formation of Te vacancies [36].

We then investigate the effect of incorporated Te vacancies on the chemical states of the Bi and Te elements in the Bi_2Te_3 material from the X-ray photoelectron spectroscopy (XPS, Fig. S2). For the XPS spectrum of Bi 4f orbital in the pristine Bi_2Te_3 material, as shown in Fig. 1c, the peaks at 158.98 and 164.28 eV represent the Bi $4f_{7/2}$ and Bi $4f_{5/2}$ of Bi_2Te_3, while the peaks at 158.78 and 164.08 eV are consistent with the Bi 4f spectrum of the Bi_2Te_3 oxide layer [37]. For the XPS spectrum of Te 3d orbital in the pristine Bi_2Te_3 material (Fig. 1d), the peaks at 575.88 and 586.28 eV correspond to the Te $3d_{5/2}$ and Te $3d_{3/2}$ of Bi_2Te_3, respectively, while the peaks at 575.38 and 585.78 eV are originated from Te–O bonding [38]. The oxidation peaks of Bi–O and Te–O observed in the XPS spectra could be attributed to the sample preparation and drying processes. During the hydrothermal synthesis at 180 °C, the presence of oxygen in the reaction chamber might cause sample oxidation. Furthermore, the samples could undergo additional oxidation during the drying process at 80 °C. Consequently, the XPS spectra display oxidation peaks that correspond to Bi–O and Te–O bonds. However, this oxidation layer may be amorphous, which is why the XRD data do not indicate any oxide components. The surface oxidation behavior of synthesized Bi_2Te_3 nanomaterial has also been noted in previous literature [39,40]. In comparison, the XPS spectra of Bi 4f and Te 3d orbitals of H-Bi_2Te_3 exhibit a shift to lower binding energies relative to pure Bi_2Te_3. The reduction in the binding energies of Bi and Te with $NaBH_4$ treatment can be explained as follows. The $NaBH_4$ treatment introduces Te vacancies in Bi_2Te_3, forming the Bi_2Te_{3-x}. The introduction of Te vacancies results in a diminished coordination number of metal ions proximate to the Te vacancy, subsequently reducing the effective positive charge of these metal ions. Moreover, these Te vacancies instigate local lattice distortions and strains near the vacancy, which initiate lattice relaxation and augment the local Bi–Te bond length. This elongation implies a weakening of the bond energy. Consequently, we observed a decrease in the binding energy of both Bi and Te in the H-Bi_2Te_3 material.

To further investigate the vacancy structure in H-Bi_2Te_3 and ascertain the successful introduction of vacancies, an electron paramagnetic resonance (EPR) spectroscopy study was conducted (Fig. 1e). It was found that the H-Bi_2Te_3 nanosheets exhibited a strong electron resonance peak near 3517 G, corresponding to an effective g-value of 2.003, which can be attributed to unpaired electrons captured by Te vacancies [41]. The inductively coupled plasma optical emission spectrometry (ICP-OES) data confirm that the defective H-Bi_2Te_3 material possesses a high ratio of Te vacancies of ca. 38% (Table S2).

We subsequently observed the fine-scale morphology of the pristine Bi_2Te_3 and defective H-Bi_2Te_3 materials using scanning electron microscopy (SEM) and transmission electron microscopy (TEM) characterizations (Fig. 2). Both the pristine Bi_2Te_3 and H-Bi_2Te_3 materials show layered structures in the SEM images (Fig. 2a, d). The TEM images (Fig. 2b, e) reveal a hexagonal structure in both the pristine Bi_2Te_3 and defective H-Bi_2Te_3. The high-resolution TEM (HRTEM) images reveal the arrangement of atoms in Bi_2Te_3 and H-Bi_2Te_3 (Fig. 2c, f),

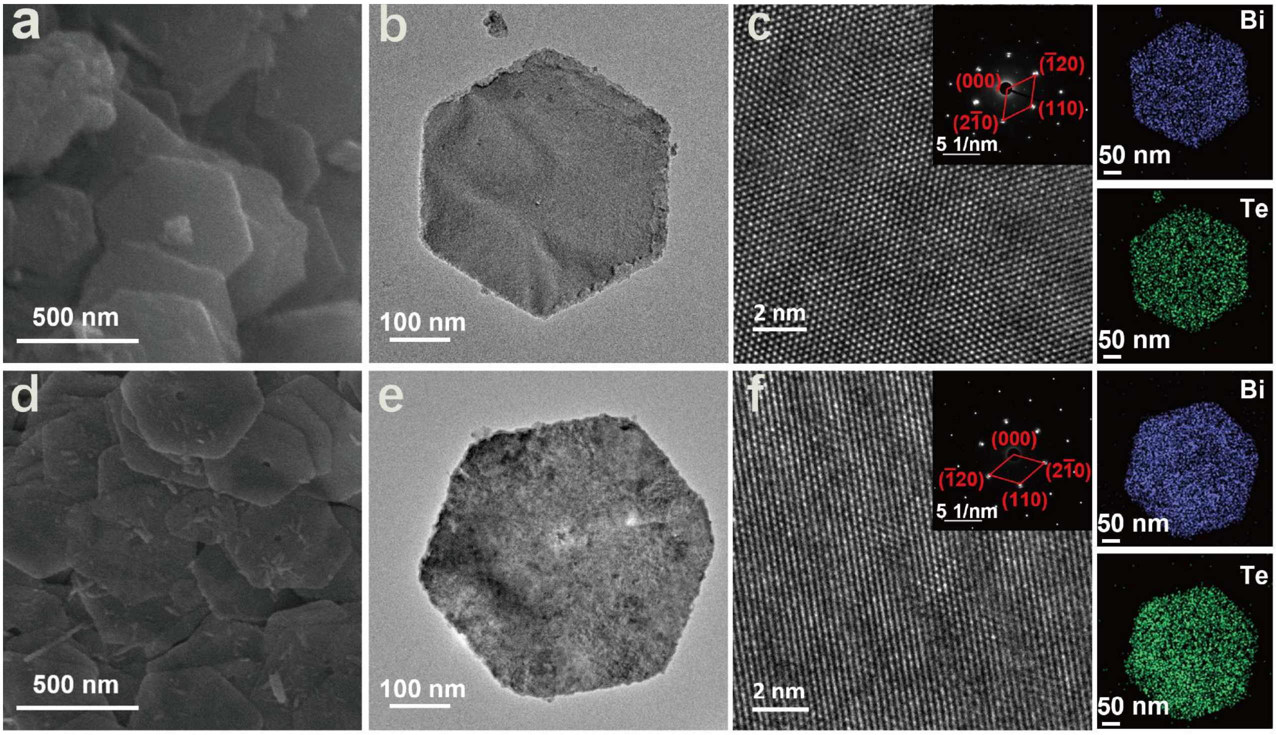

Figure 2 (a) SEM image, (b) TEM image, (c) HRTEM image, SAED pattern, and EDS-mapping results of the pristine Bi_2Te_3. (d) SEM image, (e) TEM image, (f) HRTEM image, SAED pattern, and EDS-mapping results of the defective H-Bi_2Te_3.

showing rhombohedral phases along the (110) plane. Selective area electron diffraction (SAED) patterns corresponding to (110), ($\bar{1}$20) and (2$\bar{1}$0) crystal planes indicate the existence of intact crystalline structures of Bi_2Te_3 and H-Bi_2Te_3. The elemental mapping analysis shows that the Bi and Te elements are homogeneously distributed on the surface of the samples before and after treatment. These results indicate that the Te vacancy does not change the morphology and elemental mapping of Bi_2Te_3.

Electrochemical zinc ion storage performance

The well-preserved crystal structure and abundant Te vacancies of the synthesized defective H-Bi_2Te_3 material inspire us to examine its electrochemical zinc ion storage performance. For comparative purposes, the pristine Bi_2Te_3 material was also tested. Fig. 3a illustrates the cyclic voltammetry (CV) profiles of electrodes equipped with H-Bi_2Te_3 and Bi_2Te_3 at a scan rate of 0.5 mV s^{-1}. Both samples display similar peak configurations in the voltage ranges of 0.6–0.8 and 1.0–1.2 V; however, the H-Bi_2Te_3 exhibits significantly larger peak areas. This suggests that the $NaBH_4$ treatment process neither introduces new energy storage mechanisms nor changes the electrochemical reaction pathways, but notably enhances the capacitive contributions. Accordingly, as depicted in Fig. 3b under a current density of 0.1 A g^{-1}, both samples exhibit comparable voltage plateaus within the same potential windows. Notably, the Bi_2Te_3 achieves a specific capacity of 325 mAh g^{-1} at 0.1 A g^{-1}, exceeding that of the Bi_2Te_3 (170 mAh g^{-1}) by 190%. These galvanostatic charge-discharge (GCD) results align well with the CV characteristics, jointly confirming the enhanced capacity. The performance improvement is primarily attributed to the substantial Te vacancy defects generated via $NaBH_4$ treatment, which provide abundant active sites for Zn^{2+} storage.

In conjunction with the extensive active sites induced by the

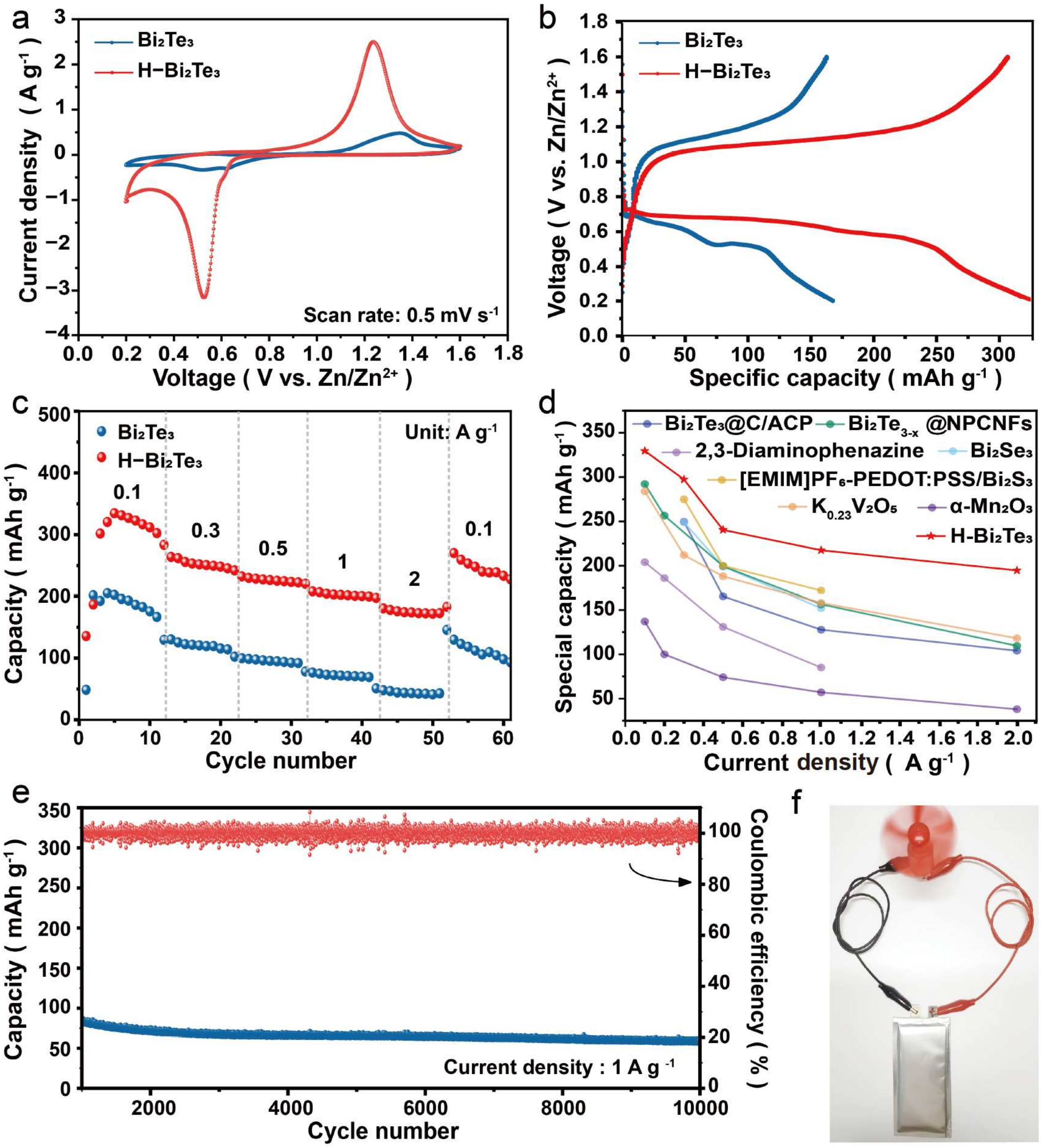

Figure 3 Electrochemical energy storage performance of the defective H-Bi_2Te_3 and pristine Bi_2Te_3 materials. (a) CV curves. (b) GCD profiles. (c) Rate performance. (d) Comparison of rate performance. (e) Cycling stability. (f) A photograph showing the assembled Zn//H-Bi_2Te_3 soft pack battery can power an electric fan.

abundant Te vacancies, the H-Bi_2Te_3 exhibits a significantly enhanced rate capability across diverse current densities (Fig. 3c). At applied current densities of 0.1, 0.3, 0.5, 1.0, and 2.0 A g^{-1}, the material yields specific capacities of 330, 297, 240, 217, and 195 mAh g^{-1}, respectively. Notably, the capacity values of H-Bi_2Te_3 significantly exceed those of the pristine Bi_2Te_3 and a range of recently reported cathode materials, encompassing oxides, sulfides, tellurides, and organics (Fig. 3d) [18,42–46].

We noticed that the capacity of the H-Bi_2Te_3 material starts low and stabilizes after about 5 cycles when tested at 0.1 A g^{-1}. This can be attributed to the processes of electrolyte wetting and material activation during the initial cycles. During the period following battery assembly, the active material may not be fully saturated by the electrolyte, resulting in poor Zn ion transport across the electrode/electrolyte interface and consequently leading to a low initial capacity. However, as cycling continues at 0.1 A g^{-1}, the active materials of H-Bi_2Te_3 are progressively fully saturated and activated, leading to capacity stabilization after approximately 5 cycles. It should also be noted that the H-Bi_2Te_3 material requires more activation cycles to reach a stabilized capacity than the untreated Bi_2Te_3 material, as depicted in Fig. 3c. The prolonged activation period and delayed stabilization of electrochemical ion storage performance in vacancy-engineered electrode materials stem from kinetic relaxation during vacancy-induced structural reorganization. For the H-Bi_2Te_3 material, during the initial Zn ion storage, the Te vacancies thermodynamically trigger local lattice reconstruction and charge redistribution. This process requires multiple cycles to achieve vacancy homogenization and interfacial ion-channel reorganization, leading to initial capacity/voltage fluctuations [47]. Concurrently, high vacancy migration barriers and reduced ion diffusion coefficients in structural reorganization regions further delay kinetic equilibrium. Thus, the H-Bi_2Te_3 cathode materials require more activation cycles in Fig. 3c.

Subsequently, we examine the operational stability of the defective H-Bi_2Te_3 material, a critical parameter for battery performance. Fig. 3e presents the endurance cycling performance of the H-Bi_2Te_3 at 1 A g^{-1}, illustrating its robust stability for electrochemical zinc ion storage. Remarkably, it retains a capacity of 70 mAh g^{-1} after 10000 cycles, all while maintaining a near-perfect Coulombic efficiency. These results and the survey on the AZIB cathode performance in Table S3 and Fig. 3d suggest that the defective H-Bi_2Te_3 material exhibits superior cathode performance for AZIBs, characterized by outstanding capacity, high rate performance, and exceptional operational stability. To further illustrate the cathode property of the H-Bi_2Te_3 material for potential application in large-scale batteries, we assembled a Zn//H-Bi_2Te_3 soft pack battery. The results indicate that the battery can stably power an electric fan, thereby demonstrating its practical usage capabilities (Fig. 3f).

We further conducted *ex situ* XRD and SEM analyses on both the pristine and cycled H-Bi_2Te_3 cathodes to investigate the material's stability after extensive cycling. As illustrated in Fig. S4, the cycled electrode displays a peak alignment that is consistent with the original material, thereby confirming the structural integrity of H-Bi_2Te_3. Additionally, we identified the formation of the byproduct $Zn_4SO_4(OH)_6·5H_2O$ post-cycling. The enduring stability of the H-Bi_2Te_3 material was further evidenced through *ex situ* SEM observations (Fig. S5). Notably, post-cycling, the cathode maintained its original morphology, with no observable cracks or detachments. Concurrently, the discharge byproduct identified as $Zn_4SO_4(OH)_6·5H_2O$ exhibited a lamellar morphology, aligning with the XRD findings and prior reports [39].

Mechanism analysis

The excellent electrochemical zinc ion storage performance of defective H-Bi_2Te_3 has prompted us to explore the underlying mechanisms. We first conducted *ex situ* XRD and XPS experiments on the pristine, fully charged, and fully discharged H-Bi_2Te_3 cathodes. As illustrated in Fig. S6, the *ex situ* XRD spectra reveal that the diffraction peaks of the H-Bi_2Te_3 electrodes remain largely consistent when charged to 1.6 V or discharged to 0.2 V, exhibiting no discernible deviation from the pristine crystalline structure. This alignment of peaks suggests that the cathode material preserves its structural integrity throughout the charge/discharge cycles.

Additionally, we observed the formation of side products identified as $Zn_4SO_4(OH)_6·5H_2O$ (PDF#78-0246) on the cathodes. The XRD data suggest that the electrochemical reactions are predominantly governed by proton insertion/extraction, rather than zinc-ion intercalation, which is consistent with previous findings [21,23]. We note that Chen *et al.* [21] revealed a triple synergistic mechanism in Bi_2Te_3. Three electrochemical processes were found to occur in the aqueous Bi_2Te_3-Zn battery: (a) proton insertion/extraction, (b) $Zn_4SO_4(OH)_6·5H_2O$ generation/decomposition, and (c) conventional Zn^{2+} insertion/extraction. Among them, the proton insertion/extraction process was predominant. This observation aligns with our *ex situ* XPS characterizations depicted in Fig. S7. After fully discharged, a Zn 2p signal, attributable to the formed byproduct of $Zn_4SO_4(OH)_6·5H_2O$ on the electrode surface, becomes evident. The intensity of the Zn 2p signal diminishes but does not vanish after the battery is fully charged. The residual Zn likely corresponds to a certain amount of electrolyte left on the electrode surface and may also be attributed to some residual $Zn_4SO_4(OH)_6·5H_2O$ due to the non-fully reversible formation/dissolution of this compound. The reversible shifts observed in Bi 4f and Te 3d XPS peaks in the H-Bi_2Te_3 electrodes across pristine, fully discharged, and charged states substantiate the proton-dominated reversible reactions.

We continue to investigate the kinetics of zinc ion storage in both defective H-Bi_2Te_3 and pristine Bi_2Te_3 materials. Fig. 4a illustrates the electrochemical impedance spectra (EIS) for both H-Bi_2Te_3 and Bi_2Te_3 electrodes. The EIS data encompass high-frequency semicircles, indicative of the charge transfer process, and low-frequency straight lines, representing the ion diffusion process. The charge transfer resistance (R_{ct}), derived from the diameter of the semicircles in the EIS curves, is marginally smaller for the defective H-Bi_2Te_3 cathode compared to the pristine Bi_2Te_3 cathode (Table S4). The H-Bi_2Te_3 cathode's EIS spectrum in the low-frequency region is more vertical, suggesting a faster ion transfer characteristic.

Consequently, the EIS data suggest that the H-Bi_2Te_3 cathode exhibits improved reaction kinetics for zinc ion storage. Fig. 4b presents the galvanostatic intermittent titration technique (GITT) charge-discharge curves for the defective H-Bi_2Te_3 and pristine Bi_2Te_3 electrodes, from which the zinc ion diffusion coefficient ($D_{Zn^{2+}}$) is calculated, as shown in Fig. 4c. The $D_{Zn^{2+}}$ of the H-Bi_2Te_3 cathode at the discharge platform is 3.98×10^{-10} cm^2 s^{-1}, significantly higher than the Bi_2Te_3 cathode's 5.01×10^{-11} cm^2 s^{-1}. This enhancement in the kinetics of zinc ion

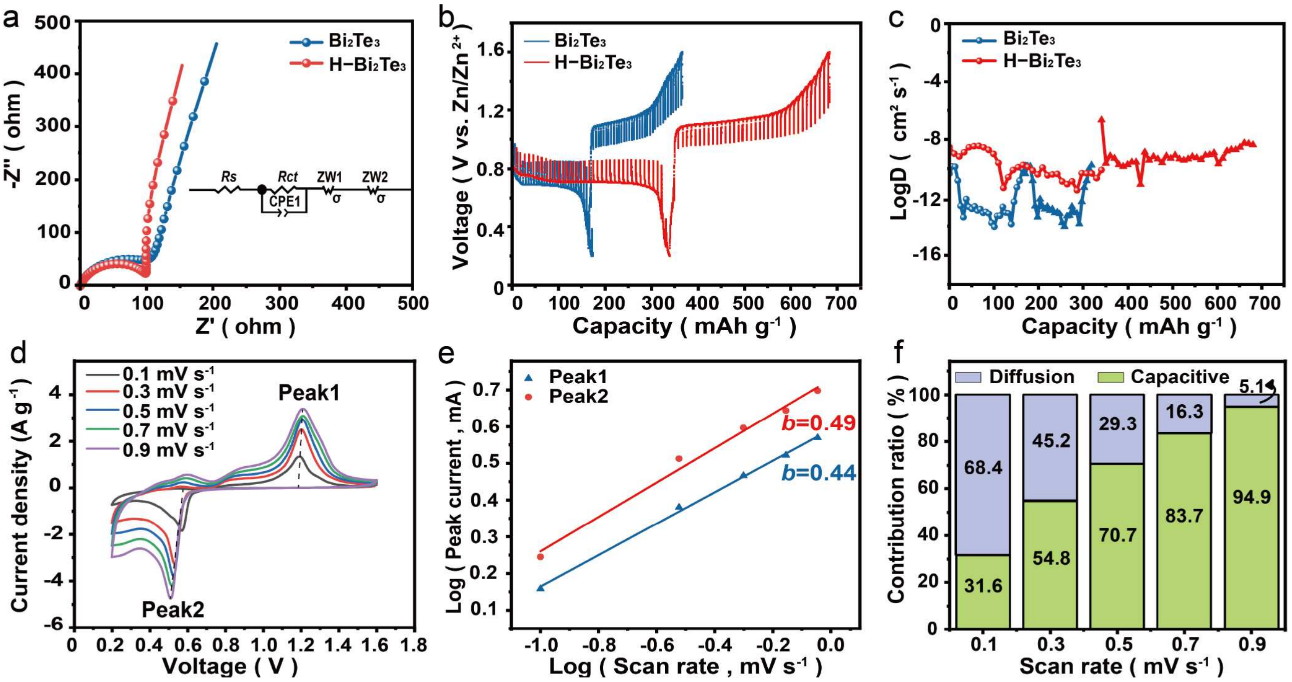

Figure 4 Zinc ion storage kinetics. (a) EIS plots and the employed circuit model for fitting [48], (b) GITT curves, (c) calculated zinc ion diffusion coefficients of the defective H-Bi_2Te_3 and pristine Bi_2Te_3 materials. (d) CV curves, (e) the corresponding plots of log(*i*, peak current) vs. log(*v*, scan rate) and (f) calculated capacitance contribution of the defective H-Bi_2Te_3 material at different sweeping rates.

transport is primarily attributed to the presence of vacancies, which effectively lower the potential barrier for interlayer diffusion, reduce the adsorption of metal ions onto zinc ions, and thereby facilitate rapid Zn^{2+} ion storage.

Fig. 4d shows the CV curves at different sweeping rates. The *b* values that reveal energy storage reaction kinetics can be calculated by the empirical power-law relationship of $i_p = av^b$ based on CV data. The *b* values for Peak 1 and Peak 2 are calculated to be 0.49 and 0.44, respectively (Fig. 4e), indicating that the energy storage process is mainly controlled by a diffusion reaction-controlled battery mechanism. The results for the pristine Bi_2Te_3 show the similar situation (Fig. S5). Further analysis was conducted to deconvolute the capacitive- and diffusion-controlled behaviors to the total current, as shown in Fig. 4f. The diffusion-dominated contribution occupies 68.4% of the total capacity at a scan rate of 0.1 mV s^{-1}. When the scan rate increases from 0.1 to 0.9 mV s^{-1}, the diffusion-controlled contribution gradually decreases to 5.1%, suggesting a clear tendency toward surface-driven capacitive storage at high scan rates.

We continually utilized density functional theory (DFT) calculations to elucidate the energy storage mechanism of the cathode materials. Fig. 5a, b present the side and top views of the layered crystal structure of Bi_2Te_3, along with the Zn^{2+} diffusion pathways within its interlayers. The movement of Zn^{2+} ions can be depicted as a sequential hopping process between adjacent octahedral (O) sites via intermediate tetrahedral (T) sites. Our DFT calculations (Fig. 5c) show that for pristine Bi_2Te_3, the energy barrier for Zn^{2+} to cross the T-site is a substantial 0.28 eV. However, when Te vacancies are introduced into Bi_2Te_3, this energy barrier decreases significantly to just 0.08 eV, thereby accelerating and making zinc ion transport more feasible. Moreover, a comparative analysis of the electronic band structures (Fig. 5d, e) reveals that these introduced Te vacancies cause a direct overlap between the conduction and valence bands in H-Bi_2Te_3, thus endowing the material with metallic characteristics. This electronic reconfiguration not only boosts bulk electronic conductivity but also synergistically enhances the overall rate capability of the electrode.

CONCLUSIONS

In summary, we have synthesized a Te vacancy-rich Bi_2Te_3 nanosheet material via a straightforward and efficient $NaBH_4$-assisted chemical reduction method. Our findings confirm that the resultant defective H-Bi_2Te_3 material maintains its layered hexagonal crystal structure, while possessing abundant Te atomic vacancies after the reduction process. Notably, this defective H-Bi_2Te_3 material demonstrates a marked enhancement in zinc ion storage attributes—including capacity, rate capability, and cycling stability—compared to the pristine Bi_2Te_3. Delving deeper, we elucidate the energy storage mechanisms underlying this superior electrochemical performance through both experimental and theoretical analyses. Experimental data indicate that H-Bi_2Te_3 showcases a significant boost in energy storage reaction kinetics, characterized by reduced electron/ion transfer resistance and a heightened zinc ion diffusion coefficient relative to the untreated Bi_2Te_3. DFT calculations further reveal that the H-Bi_2Te_3, enriched with Te vacancies, presents a diminished zinc ion diffusion energy barrier and optimized electronic band structures with metallic traits, thereby streamlining electron and ion transport during electrochemical energy storage. This work not only offers a high-caliber cathode material for AZIBs but also holds promise for broader property tuning and application development, capita-

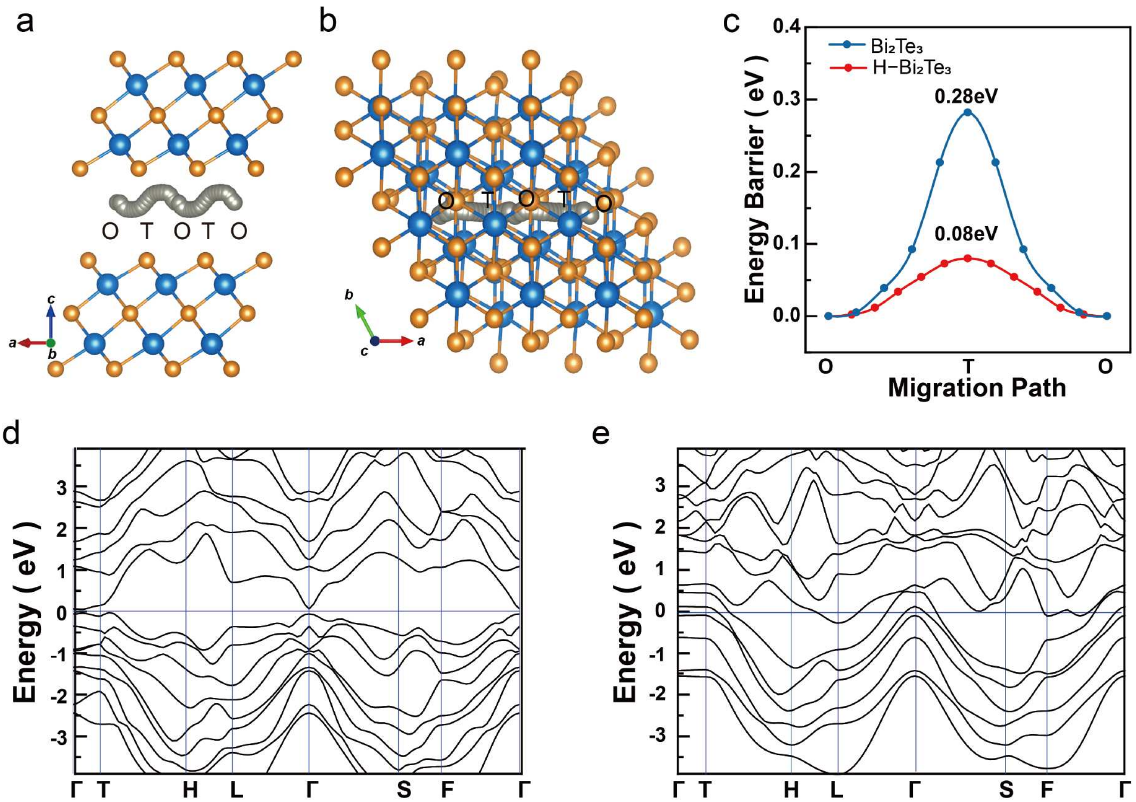

Figure 5 DFT calculations. (a) Side-view and (b) top-view of the zinc ion transport paths in the H-Bi_2Te_3 material. (c) Calculated zinc ion diffusion energy barriers in the defective H-Bi_2Te_3 and pristine Bi_2Te_3 materials. Calculated band plots of the (d) pristine Bi_2Te_3 and (e) defective H-Bi_2Te_3 materials.

lizing on vacancy defects in layered compounds.

Received 7 May 2025; accepted 23 July 2025;
published online 15 September 2025

1 Jiang L, Liu L, Yue J, *et al.* High-voltage aqueous Na-ion battery enabled by inert-cation-assisted water-in-salt electrolyte. Adv Mater, 2020, 32: 1904427
2 Mu T, Wang Z, Yao N, *et al.* Technological penetration and carbon-neutral evaluation of rechargeable battery systems for large-scale energy storage. J Energy Storage, 2023, 69: 107917
3 Liu H, Yang L, Shen T, *et al.* Distorting local structures to modulate ligand fields in vanadium oxide for high-performance aqueous zinc-ion batteries. ACS Nano, 2025, 19: 9132–9143
4 Tan Y, Pu J, Li H, *et al.* Water molecular activity management towards stable Zn anodes. Sci China Chem, 2024, 67: 4085–4097
5 Xie Y, Feng S, Gao J, *et al.* Modulating the interfacial microenvironment via zwitterionic additive for long-cycling aqueous Zn-ion batteries. Sci China Mater, 2024, 67: 2898–2907
6 Cheng L, Zhu Q, Liang J, *et al.* Flexible electron-rich ion channels enable ultrafast and stable aqueous zinc-ion storage. ACS Appl Mater Interfaces, 2021, 13: 54096–54105
7 Jiang N, Zeng Y, Yang Q, *et al.* Deep ion mass transfer addressing the capacity shrink challenge of aqueous Zn‖MnO_2 batteries during the cathode scaleup. Energy Environ Sci, 2024, 17: 8904–8914
8 Li Y, Zhao X, Gao Y, *et al.* Design strategies for rechargeable aqueous metal-ion batteries. Sci China Chem, 2024, 67: 165–190
9 Li G, Sun L, Zhang S, *et al.* Developing cathode materials for aqueous zinc ion batteries: challenges and practical prospects. Adv Funct Mater, 2024, 34: 2301291
10 Hong H, Guo X, Zhu J, *et al.* Metal/covalent organic frameworks for aqueous rechargeable zinc-ion batteries. Sci China Chem, 2024, 67: 247–259
11 Gao X, Shi T, Zu L, *et al.* Highly stable polyaniline-based cathode material enabled by phosphorene for zinc-ion batteries with superior specific capacity and cycle life. ACS Appl Mater Interfaces, 2024, 16: 24781–24795
12 Lv T, Peng Y, Zhang G, *et al.* How about vanadium-based compounds as cathode materials for aqueous zinc ion batteries? Adv Sci, 2023, 10: 2206907
13 Zeng Y, Lu XF, Zhang SL, *et al.* Construction of Co–Mn Prussian blue analog hollow spheres for efficient aqueous Zn-ion batteries. Angew Chem Int Ed, 2021, 60: 22189–22194
14 Liu Q, Yang K, Wang Z, *et al.* One-stone-for-two-birds strategy for VSe_2 to enable high capacity and long-life zinc storage. ACS Appl Mater Interfaces, 2024, 16: acsami.4c02177
15 Li L, Jia S, Cao M, *et al.* Research progress on transition metal sulfide-based materials as cathode materials for zinc-ion batteries. J Energy Storage, 2023, 67: 107614
16 Yang M, Wang Z, Ben H, *et al.* Boosting the zinc ion storage capacity and cycling stability of interlayer-expanded vanadium disulfide through *in-situ* electrochemical oxidation strategy. J Colloid Interface Sci, 2022, 607: 68–75
17 Zhang W, Gao X, Yang X, *et al.* Further elevating the energy density of aqueous zinc-ion hybrid capacitors toward batteries through voltage-window-expansion engineering. Chem Eng J, 2023, 460: 141824
18 Zhao Y, Lu Y, Li H, *et al.* Few-layer bismuth selenide cathode for low-temperature quasi-solid-state aqueous zinc metal batteries. Nat Commun, 2022, 13: 752
19 Zhang L, Yang Z, Feng S, *et al.* Metal telluride nanosheets by scalable solid lithiation and exfoliation. Nature, 2024, 628: 313–319
20 Liu B, Wang S, Yan K, *et al.* Transition metal doping of topological insulator Bi_2Te_2Se for application in zinc-ion batteries. Chem Eng J, 2025, 506: 160246
21 Chen L, Nie H, Zhou S, *et al.* Charge storage mechanism of aqueous

bismuth telluride–zinc batteries with high rate capability. Sci China Mater, 2023, 66: 3453–3460

22 Debbarma C, Radhakrishnan S, Jeong SM, *et al.* A comprehensive review on advanced supercapacitors based on transition metal tellurides: from material engineering to device fabrication. J Mater Chem A, 2024, 12: 18674–18704

23 Hou Y, Ma P, Long F, *et al.* Hierarchical porous Bi_2Te_3@C for wide-temperature-range aqueous Zn-based batteries with air-recharging capability. ACS Nano, 2024, 18: 27358–27371

24 Huang TC, Cheng KW, Lin CA, *et al.* Two-dimensional metallic VTe_2 demonstrating fast ion diffusion for aqueous zinc-ion batteries. Sustain Energy Fuels, 2022, 6: 4626–4635

25 Zhao Y, Zhang P, Liang J, *et al.* Uncovering sulfur doping effect in MnO_2 nanosheets as an efficient cathode for aqueous zinc ion battery. Energy Storage Mater, 2022, 47: 424–433

26 Li X, Wang L, Fu Y, *et al.* Optimization strategies toward advanced aqueous zinc-ion batteries: from facing key issues to viable solutions. Nano Energy, 2023, 116: 108858

27 Tay IR, Xue J, Lee WSV. Methods for characterizing intercalation in aqueous zinc ion battery cathodes: a review. Adv Sci, 2023, 10: 2303211

28 Xu W, Sun C, Zhao K, *et al.* Defect engineering activating (Boosting) zinc storage capacity of MoS_2. Energy Storage Mater, 2019, 16: 527–534

29 Fan H, Dai Y, Xue X, *et al.* Modification, application and expansion of electrode materials based on cobalt telluride. J Energy Chem, 2024, 97: 710–737

30 Zhang L, Fang D, Wang F, *et al.* Interlayer and O-vacancy engineering co-boosting fast kinetics and stable structure of hydrated sodium ammonium vanadate for aqueous zinc-ion battery. Chem Eng J, 2025, 506: 159920

31 Zhang F, Du M, Miao Z, *et al.* Oxygen vacancies and N-doping in organic–inorganic pre-intercalated vanadium oxide for high-performance aqueous zinc-ion batteries. InfoMat, 2022, 4: e12346

32 Bie Z, Jiao Z, Cai X, *et al.* Pomegranate-inspired cathodes mitigate the mismatch between carrier transport and high loading for aqueous zinc-ion batteries. Adv Energy Mater, 2024, 14: 2401002

33 Sun L, Li D, Du H, *et al.* Eu_2O_3–Cu/NC nanocomposite catalyst with improved oxygen reduction reaction activity for Zn-air batteries. Int J Hydrogen Energy, 2021, 46: 3974–3983

34 Jiang C, Zhang L, Gao X, *et al.* Se-vacancy porous ultrathin ZnSe nanosheet/carbon composite for sodium storage via electron beam irradiation strategy. Chem Eng J, 2024, 497: 154936

35 Zhao D, Zhu Q, Li X, *et al.* Oxygen vacancies of commercial V_2O_5 induced by mechanical force to enhance the diffusion of zinc ions in aqueous zinc battery. Batteries Supercaps, 2022, 5: e202100341

36 Shin H, Seo J, Jeon SH, *et al.* Enhanced catalytic activity and stability of SOFC electrodes through plasma-driven surface modification. J Mater Chem A, 2024, 12: 10695–10703

37 Yin K, Cui ZD, Zheng XR, *et al.* A Bi_2Te_3@CoNiMo composite as a high performance bifunctional catalyst for hydrogen and oxygen evolution reactions. J Mater Chem A, 2015, 3: 22770–22780

38 Liu X, Si Y, Li K, *et al.* Exploring sodium storage mechanism of topological insulator Bi_2Te_3 nanosheets encapsulated in conductive polymer. Energy Storage Mater, 2021, 41: 255–263

39 Zeng G, Sun Q, Horta S, *et al.* A layered Bi_2Te_3@PPy cathode for aqueous zinc-ion batteries: mechanism and application in printed flexible batteries. Adv Mater, 2024, 36: 2305128

40 Wang Q, Wang S, Wei N, *et al.* Aqueous zinc-ion batteries based on a 2D layered Bi_2Te_3 cathode. Chem Eng J, 2022, 450: 138132

41 Gong Q, Yang D, Yang H, *et al.* Cobalt ditelluride meets tellurium vacancy: an efficient catalyst as a multifunctional polysulfide mediator toward robust lithium–sulfur batteries. ACS Nano, 2024, 18: 28382–28393

42 Zhao Y, Ma L, Zhu Y, *et al.* Inhibiting grain pulverization and sulfur dissolution of bismuth sulfide by ionic liquid enhanced poly(3,4-ethylenedioxythiophene):poly(styrenesulfonate) for high-performance zinc-ion batteries. ACS Nano, 2019, 13: 7270–7280

43 Wang Q, Liu Y, Chen P. Phenazine-based organic cathode for aqueous zinc secondary batteries. J Power Sources, 2020, 468: 228401

44 Wang G, Li Q, Zhang W, *et al.* Unveiling the synergy of architecture and anion vacancy on Bi_2Te_{3-x}@NPCNFs for fast and stable potassium ion storage. ACS Appl Mater Interfaces, 2024, 16: 13858–13868

45 Zhang W, Tang C, Lan B, *et al.* $K_{0.23}V_2O_5$ as a promising cathode material for rechargeable aqueous zinc ion batteries with excellent performance. J Alloys Compd, 2020, 819: 152971

46 Guo Y, Zhao Z, Zhang J, *et al.* High-performance zinc-ion battery cathode enabled by deficient manganese monoxide/graphene heterostructures. Electrochim Acta, 2022, 411: 140045

47 Wang C, Liu L, Zhao S, *et al.* Tuning local chemistry of P2 layered-oxide cathode for high energy and long cycles of sodium-ion battery. Nat Commun, 2021, 12: 2256

48 Sun T, Zheng S, Nian Q, *et al.* Hydrogen bond shielding effect for high-performance aqueous zinc ion batteries. Small, 2022, 18: 2107115

Acknowledgement This work was financially supported by the National Key Research and Development Program of China (2021YFB2400400) and the National Natural Science Foundation of China (52171203, 52371214, and 52302224).

Author contributions Hu L designed the experiments and led the project. Tang Z and Ju N synthesized the samples and conducted most materials characterizations and electrochemical tests. Deng Z, Zhu Z, Meng H, Chen W and Ye F helped with data analysis. Du Y performed DFT calculations. Tang Z, Chen W, and Hu L wrote the paper with the support from Wu Y. All authors contributed to the general discussion.

Conflict of interest The authors declare that they have no conflict of interest.

Supplementary information Supplementary materials are available in the online version of the paper.

Zhoujie Tang is presently an undergraduate student enrolled in the School of Materials Science and Engineering, Southeast University. Her research interests are primarily centered on developing high-performance cathode materials for aqueous zinc-ion batteries.

Wenshu Chen earned his PhD degree in materials science and engineering from Shanghai Jiao Tong University in 2019. He is presently an associate professor at the School of Materials Science and Engineering, Southeast University. His primary research interests focus on electrochemical energy storage, particularly aqueous batteries.

Linfeng Hu is currently a full professor at Southeast University. He got his PhD degree from Tsukuba University/NIMS (National Institute for Materials Science, Japan) in 2010. Now his research focuses on the design of novel cathode/electrolyte materials for various aqueous batteries (Zn-ion, ammonium ion, Fe-ion, etc.) and their ion transport kinetics, energy storage mechanisms.

Yuping Wu is the chair professor of Southeast University, Fellow of Royal of Chemistry (FRSC), executive dean of Z Energy Storage Center. He got his PhD degree in 1997 from the Chinese Academy of Sciences. He was awarded as one of the Most Influential Minds over the World in 2015 (less than 20 every year) by Thomson Reuters from the Highly Cited Researchers. His main research work is on electrochemical energy storage systems and their key materials. His research led to some edge-cutting technologies such as nonporous separators for lithium batteries, hybrid supercapacitors, and aqueous rechargeable lithium batteries.

具有丰富Te空位的Bi_2Te_3作为一种高性能水系锌离子存储正极材料

汤周婕[1], 陈文书[1*], 邓郅泷[1], 朱子悦[1], 孟灏圆[1], 居娜[1], 叶飞[2],
杜永平[3], 吴宇平[4,5], 胡林峰[1,5*]

摘要 层状过渡金属碲化物(TMT)展现出发展为水系锌离子电池高性能正极材料的潜力，但其整体性能指标(如比容量、倍率性能、稳定性等)与实际应用仍存在显著差距．在此，我们采用一种简单高效的$NaBH_4$辅助的化学刻蚀方法，在Bi_2Te_3表面构建了丰富的Te空位(H-Bi_2Te_3). 实验和理论研究表明, 丰富的Te空位优化了H-Bi_2Te_3的能带结构, 提升了其电导率, 并显著降低了锌离子的扩散势垒. 此外, Te空位为锌离子提供了更多的存储位点. 因此，H-Bi_2Te_3材料在锌离子存储方面表现出快速的锌存储动力学($D_{Zn^{2+}}$为3.98×10^{-11} cm^2 s^{-1})、高的比容量(0.1 A g^{-1}时达325 mAh g^{-1})、出色的倍率特性(1 A g^{-1}时为217 mAh g^{-1})以及优异的循环稳定性(1 A g^{-1}下循环10000次后仍具有70 mAh g^{-1}的容量)．这项工作不仅为水系锌离子电池中基于TMT的正极材料改性提供了一种聚焦于空位缺陷工程的新策略，也为探索富空位TMT材料的更广泛应用开辟了可能性.